Nuclear Instruments and Methods in Physics Research B70 (1992) 286–297
North-Holland

NIM B
Beam Interactions with Materials & Atoms

The GSI projectile fragment separator (FRS): a versatile magnetic system for relativistic heavy ions

H. Geissel, P. Armbruster, K.H. Behr, A. Brünle, K. Burkard, M. Chen [1], H. Folger, B. Franczak, H. Keller, O. Klepper, B. Langenbeck, F. Nickel, E. Pfeng, M. Pfützner [2], E. Roeckl, K. Rykaczewski [2], I. Schall, D. Schardt, C. Scheidenberger, K.-H. Schmidt, A. Schröter, T. Schwab, K. Sümmerer, M. Weber and G. Münzenberg
Gesellschaft für Schwerionenforschung, D-6100 Darmstadt, Germany

T. Brohm, H.-G. Clerc, M. Fauerbach, J.-J. Gaimard, A. Grewe, E. Hanelt, B. Knödler, M. Steiner, B. Voss, J. Weckenmann and C. Ziegler
Inst. für Kernphysik, TH Darmstadt, D-6100 Darmstadt, Germany

A. Magel and H. Wollnik
Universität Gießen, D-6300 Gießen, Germany

J.P. Dufour
CEN, Bordeaux, F-33175, France

Y. Fujita
College of General Education, Osaka University, Toyonaka, Osaka 560, Japan

D.J. Vieira
Los Alamos National Laboratory, Los Alamos, NM 87545, USA

B. Sherrill
NSCL, East Lansing, MI 48824, USA

The projectile fragment separator FRS designed for research and applied studies with relativistic heavy ions was installed at GSI as a part of the new high-energy SIS/ESR accelerator facility. This high-resolution forward spectrometer has been successfully used in first atomic and nuclear physics experiments using neon, argon, krypton, xenon, and gold beams in the energy range from 500 to 2000 MeV/u. For the first time relativistic xenon and gold fragments have been isotopically separated. In this contribution we describe first experiments characterizing the performance of this spectrometer.

1. Introduction

Heavy-ion research at GSI has been extended to relativistic energies with the new synchrotron SIS [1], the projectile FRagment Separator FRS [2], and the Experimental Storage and cooler Ring ESR [3] (see fig. 1). The SIS can accelerate all ions, from hydrogen to uranium, to a maximum magnetic rigidity of 18 Tm which corresponds to energies of 1–4.5 GeV/u. The main beam parameters of the SIS are summarized in table 1. Secondary beams of radioactive isotopes can be produced via projectile fragmentation with a high rate and can be efficiently separated by the FRS. The

[1] On leave from: SINR Shanghai, P.R. China.
[2] On leave from: Institute of Experimental Physics, Warsaw University, PL-00-682 Warsaw, Poland.

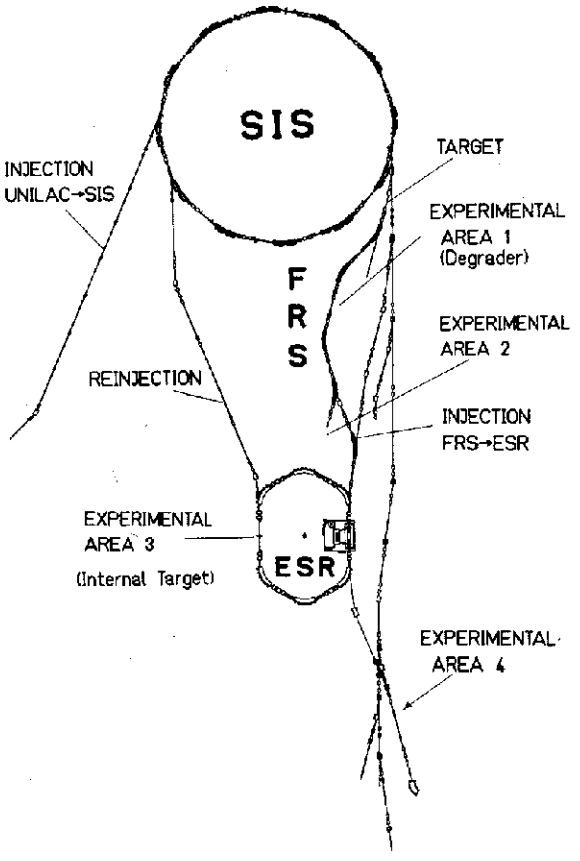

Fig. 1. Layout of the new high-energy facilities at GSI. The heavy-ion synchrotron SIS can accelerate all ions from H to U with energies up to 1–4.5 GeV/u. The projectile separator FRS in combination with the storage and cooler ring ESR can provide highly brilliant radioactive beams to all experimental areas.

fragments separated in-flight can be studied directly at the final focal plane of the FRS, or they can be injected into the ESR for experiments in the ring. The cooling facilities of the ESR [4], drastically increase the phase-space density of the radioactive beam, and a variety of unique high-resolution experiments are possible. Moreover, such cooled secondary beams can then be extracted from the ESR and delivered to the different experimental facilities shown in fig. 1.

Table 1
SIS beam parameters

Ions	all ions from H to U
Energy	1–4.5 GeV/u $B\rho_{max} = 18$ Tm
Intensity	2×10^{11}/spill (Ne^{10+}) (presently 10^9/spill)
	4×10^{10}/spill (Au^{64+}) (presently 10^6/spill)
Emittance	$\epsilon_x = \begin{cases} 1\text{–}5\pi \text{ mm mrad (slow extraction)} \\ 5\text{–}20\pi \text{ mm mrad (fast extraction)} \end{cases}$
	$\epsilon_y = 5\text{–}20\pi$ mm mrad
Time structure	10–4000 ms (slow extraction)
	20– 50 ns (fast extraction)
Momentum spread	$< 10^{-3}$

2. Design and technical layout

The FRS is an achromatic magnetic forward spectrometer with a momentum resolving power of 1500 for an emittance of 20π mm mrad. Heavy-ion beams with magnetic rigidities from 5 to 18 T m can be analyzed by the device. The location within the SIS-ESR complex was determined by the requirement of using the FRS in combination with both instruments. The system has four independent stages, each consisting of a 30° dipole magnet and a set of quadrupoles before and after the dipole to fulfill first-order focussing conditions; see fig. 2. The quadrupole magnets in front of the dipole magnets are adjustable to properly illuminate the field volume of the bending magnets to achieve a high resolving power and to minimize the vertical gap width and thus minimizing the price of the dipole magnets. The quadrupoles following the dipole magnets determine the ion-optical conditions at the four focal planes F_1 to F_4 indicated in the upper part of fig. 2, where the magnetic elements and the particle envelopes are schematically presented for an emittance of 20π mm mrad and a beam spot of 2.7 mm. In the achromatic mode of operation point-to-point images in the x direction (i.e., in the direction of dispersion) are required at all four focal planes while waists in the y direction (i.e., the direction perpendicular to both the x and the optical axis) are required only at F_2 and F_4. The dashed line in the figure indicates the ray for the momentum deviation of 1% demonstrating that the maximum dispersion (−6.8 cm/%) is reached at the central focal plane. Moreover, it is required that the angular divergence at this position does not depend on the momentum deviation of the beam at the entrance of the FRS, manifested by a parallel dispersion line ($(x' \mid \delta p) = 0$). The achromatic condition for this tune is realized at the final focal plane by requiring that both the image size and the angular divergence are independent (to first order) of the momentum spread of the incident beam (i.e., $(x \mid \delta p) = 0$, $(x' \mid \delta p) = 0$).

The ion-optical system can be corrected for second-order aberrations by using sextupole magnets placed in front of and behind each dipole magnet. These positions have been determined by the magnitudes of the corresponding coupling coefficients following the procedure proposed by Brown [5]. The required sextupole fields are relatively low, implying that the induced aberrations of third and higher order are minimized. Results of ray-tracing calculations predict that more than 90% of the first-order momentum resolution is restored for a beam characterized by a

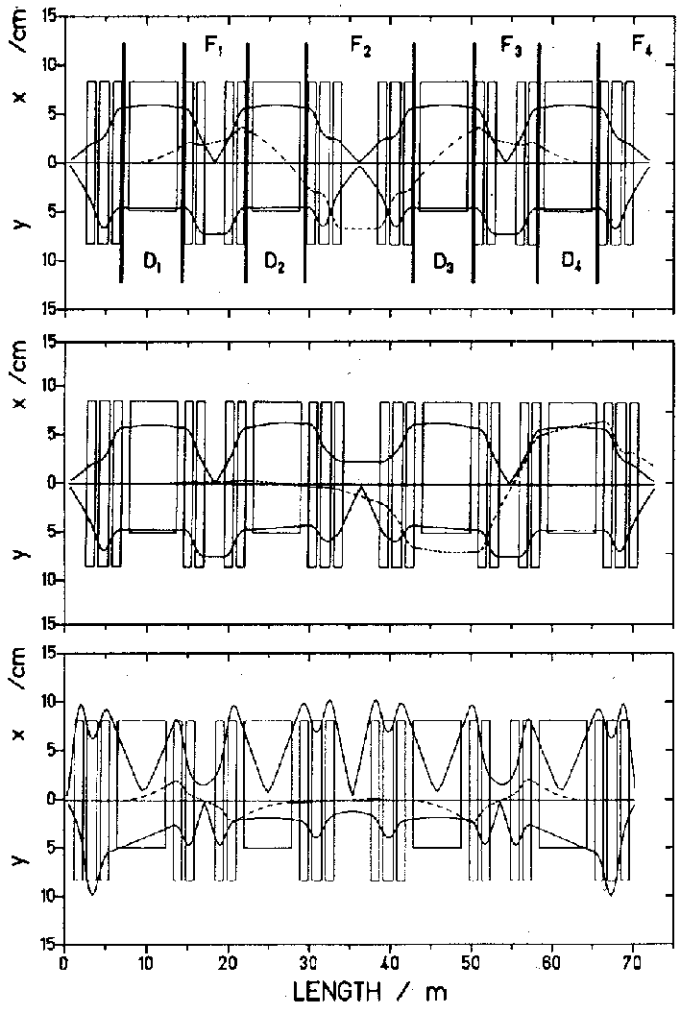

Fig. 2. Ion-optical elements of the FRS tuned for different operation modes. The 30° dipole magnets are indicated by D_1–D_4 and the different focal planes by F_1–F_4. The quadrupole magnets are placed in front of and behind the dipoles. The upper part of the figure shows the high-resolution achromatic mode, the next part the high-dispersion mode, and the lower part the high-transmission mode. The sextupole magnets are only shown in the schematic plot for the high-resolution achromatic mode. The envelopes for the standard achromatic and the high-dispersion modes are 20π and 40π mm mrad in the x and y directions, respectively, while the corresponding envelopes for the high acceptance mode are 220π and 50π mm mrad. The beam spot was 2.7 mm. The momentum deviation of 1% is indicated by dashed lines in the upper and lower part of the figure, whereas for the high-dispersion mode the momentum deviation is 0.1%. The y axis is simultaneously the negative direction for the dispersion lines.

transverse emittance of 20π mm mrad and a momentum spread of 2%, which represents the design acceptance of the FRS tuned in the achromatic ion-optical mode described above. Furthermore, the sextupole fields are needed to rotate the focal plane at F_2 so that it is perpendicular to the optical axis. In table 2, the main ion-optical parameters of the described mode are presented.

The FRS can be used as an energy-loss spectrometer as well. Precise measurements of energy transfers in nuclear and atomic reactions are possible with such a spectrometer independent of the relatively large momentum spread of the incident beam. In this mode of operation the target is placed in the central focal plane; the other settings are identical to that of the achromatic mode.

Each FRS magnet is equipped with an independent power supply allowing maximum flexibility in order to adapt the ion-optical conditions to the specific requirements of different experiments. The FRS has two target stations at different distances from the entrance quadrupole triplet. To achieve a high momentum resolution at the dispersive focal planes, the corresponding distance of the first target station is 2.20 m. The second one, positioned at 0.90 m, allows a larger acceptance at the expense of momentum resolution. The operating parameters for the two achromatic modes are summarized in table 3.

In the modes of achromatic operation described above the momentum dispersions of the first and the second dipole stages are cancelled by that of the third and the fourth, so that the overall system from target to F_4 is achromatic. Applications which neither require the achromatic condition nor a large transmission can take advantage of the possibility to double the momentum resolution. In this high dispersion mode of the FRS, a parallel beam is required in x at the centre (see middle part of fig. 2 and table 3).

An extreme operation mode that achieves a large acceptance combined with a modest resolving power is presented in the lower part of fig. 2. The selected conditions are such that at the second and final focal planes the system is achromatic and the dispersion line crosses zero at the first and third foci (see table 3, high acceptance mode). This exotic mode has already been successfully used in an experiment searching for antiprotons produced in subthreshold central collisions of 2000 MeV/u Ne projectiles impinging on NaF and Cu targets [6].

For injection into the ESR [7] the second exit of the FRS is chosen (see fig. 3). It consists of a quadrupole triplet illuminating a 30° dipole magnet and two additional quadrupole doublets as needed to achieve the final focus conditions and to additionally perform the phase-space matching of the two ion-optical systems. Furthermore, a small 7° dipole magnet D_3' is needed to allow for more space between the FRS dipole D_4' and the entrance of the ESR.

The technical design and operation of the FRS is fully integrated into the SIS-ESR system. The magnets are laminated although they will be used only in dc operation. Besides the reduced purchase costs, the

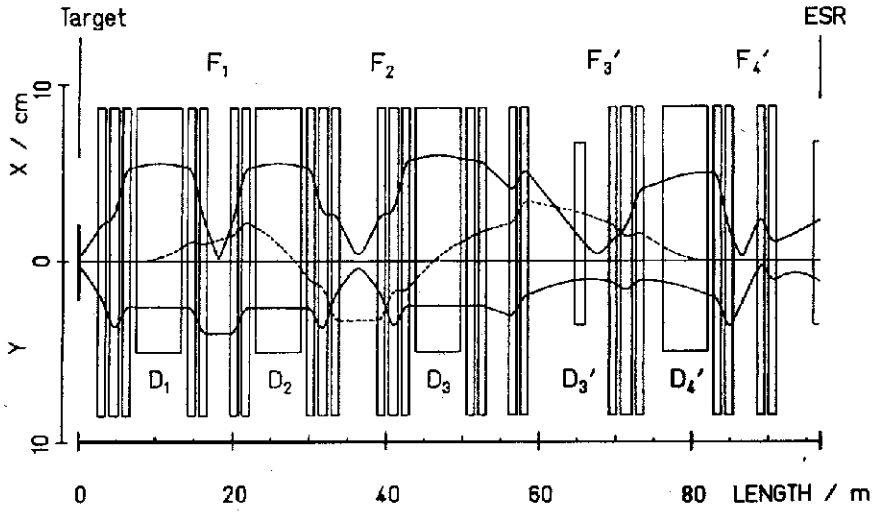

Fig. 3. Ion-optical elements of the FRS for the injection into the ESR. The envelopes are shown for an emittance of 20π mm mrad and the dispersion line for 0.5% momentum deviation.

Table 2
Calculated ion-optical matrix elements of the standard high-resolution achromatic mode at the central and final focal planes

Matrix element	At F_2	At F_4
$(x \mid x)$	0.79	1.00
$(x \mid x')$ [cm/mrad]	0	0
$(x \mid \delta p)$ [cm/%]	−6.81	0
$(x' \mid x)$ [mrad/cm]	1.21	1.92
$(x' \mid x')$	1.27	1.00
$(x' \mid \delta p)$ [mrad/%]	0	0
$(y \mid y)$	−1.13	0.83
$(y \mid y')$ [cm/mrad]	−0.007	0.011
$(y' \mid y)$ [mrad/cm]	12.32	−27.84
$(y' \mid y')$	−0.81	0.83

laminated magnets are advantageous for experiments demanding frequent changes of field settings. The H-type 30° dipole magnets can be operated up to a maximum field of 1.6 T and are controlled by calibrated Hall probes. The precision and stability of the probes is about 10^{-4} T. All magnets have been carefully field-mapped over the full range of operation. The resulting current–field relations as well as the effective lengths are used as input parameters for our ion-optical codes and operation procedures.

Each of the two target stations of the FRS is equipped with a water-cooled ladder which holds up to 15 targets of 20 mm diameter. Details of the target techniques used in this high-radiation area are described in ref. [8]. A secondary-electron detector

Table 3
Comparison of different ion-optical modes of the FRS. The accepted solid angles (Ω) are shown for the corresponding emittances (ϵ) and accepted momentum deviations. The momentum resolving power, the magnification ($(x \mid x)$), and the dispersion coefficient ($(x \mid \delta p)$) are presented for the different operation modes. See also fig. 2

Operation mode		Standard achromatic		Dispersive	High acceptance
Target distance [m]		2.2	0.90	2.20	0.90
x [mm]		±2.7	±2.7	±2.7	±2.7
ϵ_x [π mm mrad]		20	200	20	220
$(\Delta p/p)_{acc}$ [%]		2	2	0.05	2
Ω [msr]		0.32	3.4	0.32	4.6
$B\rho_{max}$ [T m]		18	8.6	18	8.3
Resolving power	at F_2	1600	160	–	0
	at F_4	0	0	3300	0
$(x \mid x)$	at F_2	0.79	−7.7	parallel	0.65
	at F_4	1.00	1.00	−0.95	−0.77
$(x \mid \delta p)$ [cm/%]	at F_2	−6.81	−6.57	−12.7	0
	at F_4	0	0	17.1	0

(SEETRAM) [9] placed upstream of the first target station can measure high beam intensities exceeding the rate limitations of single-particle counting. In the target area and also at each focal plane, two-dimensional grids with gas amplification and current readout are used for beam alignment [10]. They are especially needed when fast-extracted beams from the SIS are used in combination with the ESR. The particle detection in the FRS for slowly-extracted beams is performed by using multiwire proportional chambers [11] installed at all the focal planes. At F_2 and F_4 pairs of these detectors placed at a distance of approximately 1 m are used for particle tracking to determine the ion-optical properties of the device and to analyze the primary beam or reaction products with respect to position, angle, and $B\rho$ value. In the achromatic mode the complete phase space of the primary beam can be determined by coincidence measurements at F_2 and F_4. Slits are available at the entrance of the FRS and at each focus. All the diagnostic elements are remotely controlled and can be removed from the optical axis via vacuum feedthroughs.

3. First experimental results

3.1. Ion-optical measurements

The ion-optical performance of the FRS was tested in the magnetic rigidity range from 4 to 18 T m using different projectile and fragment beams. High-energy light ions are well suited for ion-optical measurements using the described particle-tracking detectors because these ions suffer only relatively small energy and angular straggling in the detector material. For example, in an experiment using 1000 MeV/u ^{40}Ar we verified first-order imaging conditions and achromatism of the system by coincidence measurements between the different multiwire proportional chambers positioned at F_1 to F_4. The achromatism was verified by inserting a striped target at the entrance of the spectrometer. Particles penetrating the striped target suffered an energy loss of about 1%. They were clearly separated from ions which suffered no energy loss (i.e., missed the stripes) at the dispersive focal planes, but both ensembles were refocussed at F_4. The required conditions for the momentum dispersion at the different focal planes were also verified by tracking ions passing through the FRS in different ionic charge states. The results of these investigations are in good agreement with the design goals, e.g., the measured momentum resolution was better than 1500 for an emittance of 17π mm mrad. More detailed studies of higher-order aberrations will be performed with new tracking detectors under development which will avoid the disturbing influence of wire planes [11].

3.2. In-flight separation of relativistic projectile fragments

The main design goals of the FRS are to spatially separate the nuclear reaction products from the primary beam and to perform an efficient isotopic separation for selected projectile fragments [12]. Pioneering experiments performed at the BEVALAC [13–15] have proven that projectile fragmentation is a process well suited for the production and in-flight separation of exotic nuclei. Meanwhile, such experiments are successfully carried out at medium energies as well [16–18] using a more sophisticated degrader technique.

The kinematic properties of the projectile fragments are determined by the nuclear reaction mechanisms and the slowing-down processes in the production target. Relativistic projectile fragments, created in peripheral nuclear collisions, are characterized by narrow forward-peaked angular distributions with fragment velocities which lie close to that of the projectile. Thus a zero-degree spectrometer has high utility in accepting and separating such projectile fragments. The mass difference (ΔA) and charge difference (ΔZ) of the selected fragments with respect to the projectile are the crucial parameters determining the longitudinal momentum distribution widths at a fixed mean velocity. The contribution due to the atomic energy loss in the target scales with ΔZ^2 (Bethe theory) and the spread due to the fragmentation process with the square root of ΔA [19]:

$$\sigma(p_\parallel) = 87\sqrt{\Delta A} \quad \text{MeV}/c. \tag{1}$$

The relative contribution of both processes which are basic limitations for the acceptance and the isotopic resolution of spectrometers at medium energies, becomes smaller with increasing energy thus favouring the production and separation of relativistic beams.

In fig. 4, the FRS transmission and the momentum spread are calculated for different fragments produced by 1 GeV/u U projectiles in a 1 g/cm^2 Be target. A mass-to-charge ratio of 2.63 is assumed for reaction products in the calculation. The influence of the kinematics due to the fragmentation process is shown by a dashed line. The full line includes the atomic slowing down processes. It is clearly demonstrated that the transmission is nearly 100% up to $\Delta Z = 15$, suggesting the use of projectile beams which lie close to the A and Z of the desired secondary beam [20].

Particle identification with respect to A and Z is achieved by coincidence measurements of the energy loss (ΔE) in a MUltiple-Sampling Ionization Chamber (MUSIC) [21], the magnetic-rigidity ($B\rho$) analysis at the dispersive focal plane F_2, and the velocity determination with time-of-flight (TOF) detectors placed at F_2 and F_4. The flight path of the ions was 35 m. The design value of the $B\rho$-resolution ($\Delta B\rho/B\rho < 10^{-3}$) of the FRS was verified in several experiments using particles in the $B\rho$ range from 4 to 18 T m. The TOF

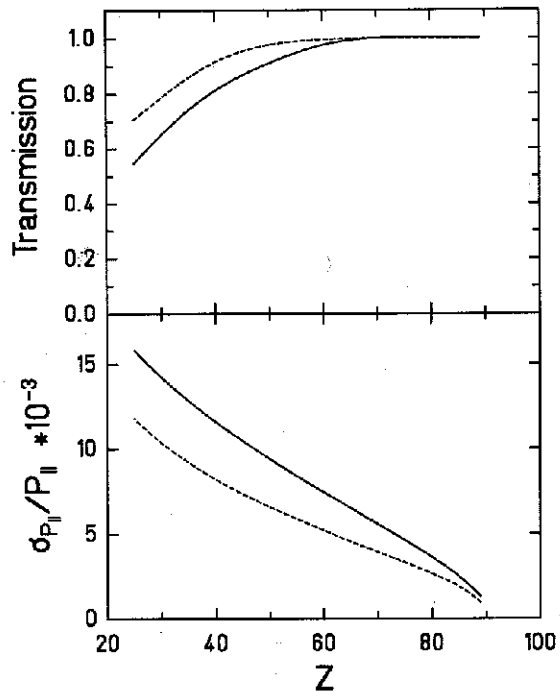

Fig. 4. Calculated momentum spread and transmission of 1 GeV/u ^{238}U fragments produced in 1 g/cm^2 Be. The dashed line indicates only the contribution due to the nuclear reaction process, while the full line includes the contribution from the energy-loss difference of the projectile and the fragment and the effect of energy-loss straggling.

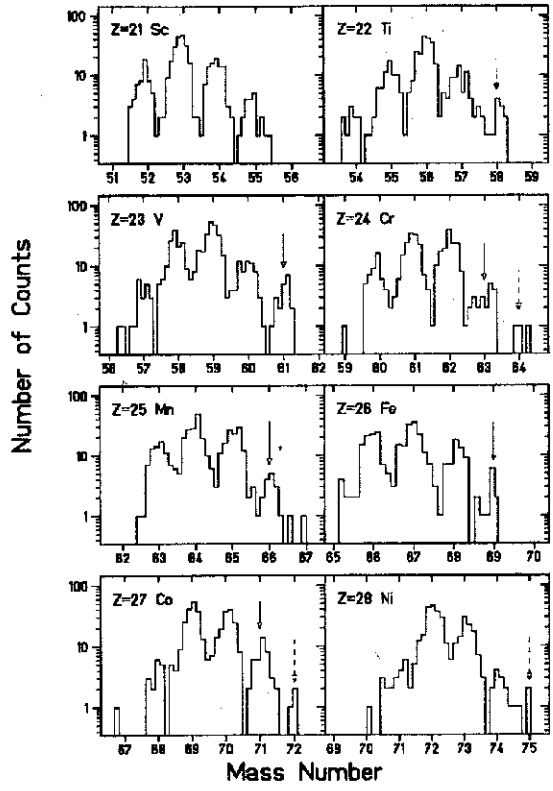

Fig. 5. Measured mass distributions of 500 MeV/u ^{86}Kr projectile fragments produced in 2 g/cm^2 Be.

was measured by two position-sensitive plastic scintillators [22] with an intrinsic time resolution of about 100 ps (FWHM). The MUSIC placed at the final focal plane reached a Z resolution of $\Delta Z = 0.3$ (FWHM) as proven in experiments with projectile fragments up to Au. The experimental results confirm that the FRS in combination with the TOF and the MUSIC detectors is capable of identifying all particles up to the heaviest fragments.

The method for particle identification described above has been applied successfully in systematic measurements of the nuclear cross section distributions using Ar, Kr, Xe, and Au projectiles with energies of 500–1000 MeV/u. Fig. 5 shows the measured mass distribution of elements $20 < Z < 29$ produced via fragmentation of 500 MeV/u ^{86}Kr in a 2 g/cm^2 Be target [23]. The $B\rho$ setting of the FRS was 11% larger than the one measured for the primary beam after passage through the production target. In this measurement we were able to unambiguously identify the exotic neutron-rich isotopes ^{71}Co, ^{69}Fe, ^{66}Mn, ^{63}Cr, ^{58}Ti, and ^{61}V as indicated by arrows in fig. 5. In view of the low ^{86}Kr beam intensity (5×10^7/spill) this result demonstrates the power of such a separation system. Preliminary results on the existence of these nuclei have also been reported in ref. [24].

Reliable predictions of nuclear fragmentation cross sections are of crucial importance in planning future experiments at the FRS. Sümmerer et al. [25] have therefore developed an empirical parametrization (EPAX) based mainly on radiochemical data of proton-induced target spallation. The cross sections measured for the ^{86}Kr + Be reaction are compared with EPAX predictions in fig. 6. The number of incident projectiles was measured with the SEETRAM detector

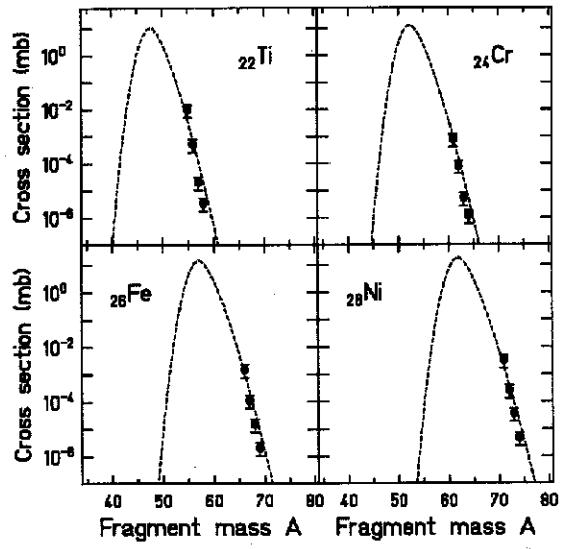

Fig. 6. Measured production cross sections of neutron-rich isotopes of Ti, Cr, Fe, and Ni as created via fragmentation of 500 MeV/u ^{86}Kr in Be. The data are compared with the empirical parametrization EPAX [25].

and the total transmission was calculated with a computer code [26]. The agreement between the experimental results and EPAX (dashed line) is excellent for these light neutron-rich nuclei, justifying the confidence in our predictions for the production rates of more exotic nuclei.

3.3. Preparation of secondary beams

For many investigations it is necessary that the selected radioactive beam is spatially separated from all other reaction products. Due to the relativistic velocities of the projectile fragments, a separation by A and Z is not possible using only electric or magnetic sector fields [2]. Therefore we have chosen a method based on a combination of magnetic rigidity analysis and atomic energy loss of the fragments in matter. The principle of separation as adapted to FRS is schematically presented in fig. 7. The keys to isotopic separation are an achromatic ion-optical system characterized by a high momentum resolving power and a profiled energy degrader placed at the dispersive focal plane F_2 [2,27–30]. The first two dipole stages of the FRS perform an A/Z selection for fully ionized reaction products, i.e. the fragments with the same magnetic rigidity are focussed on the same position of the energy degrader. The different atomic energy loss of the ions penetrating the degrader provides the additional selection criterion needed for the separation of a selected nuclide ($B\rho$–ΔE–$B\rho$ method). An experimental result demonstrating the separation method is presented in the lower part of fig. 7. In this experiment the FRS was tuned on ^{18}F produced by fragmentation of 500 MeV/u ^{40}Ar in a 2 g/cm^2 Be target. The result of the first and second selections is clearly demonstrated: the combination of the two-fold $B\rho$-analysis and the energy-loss characteristic in the F_2-degrader (11 g/cm^2 Al) provides a secondary beam of ^{18}F with only a few contaminants. The best spatial separation can be obtained with a degrader shape which preserves the achromatism of the spectrometer.

Moreover, the shape of the degrader and the characteristics of the ion-optical system can be used for interesting phase-space modelling of the fragment beam [30]. Profiled matter placed in dispersive ion-optical systems can perform quite complex transformations within the different coordinates (position, angle, and energy) of the fragment beam. The basic features of this non-Liouvillian optics can be discussed in terms of transformation matrices (so-called σ-matrix formalism [5]) in which the straggling processes of the particles are included by convolution procedures [26,30]. For detailed preparations of an experiment at FRS using the $B\rho$–ΔE–$B\rho$ separation method, a Monte Carlo code MOCADI, which includes both higher-order optics and the atomic and nuclear interaction processes, was developed [26].

By changing ion-optical parameters such as the magnification or dispersion of the FRS stages in front of and behind the degrader, or the mechanical profile of the degrader, it is possible to realize the desired imaging conditions. Two main solutions were developed for energy bunching and for achromatic focussing in the x direction, respectively. In our experiments it was more practical to mainly change the degrader shape and to work with fixed ion-optical conditions.

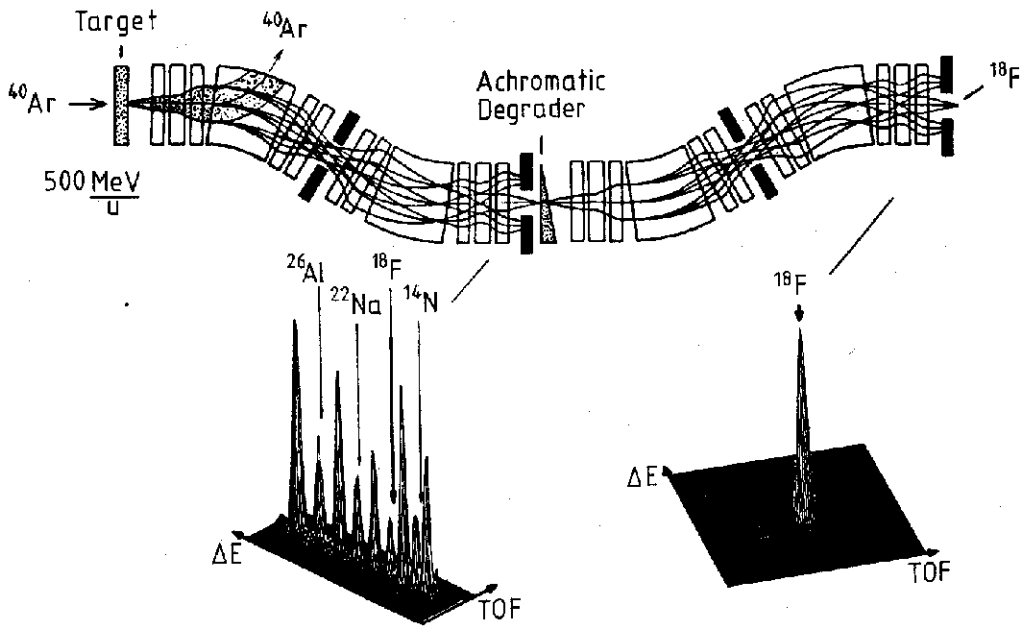

Fig. 7. The isotopic separation principle of the FRS, illustrated by measured fragment distributions produced by ^{40}Ar projectiles. The goal of this experiment was to separate and implant ^{18}F ions.

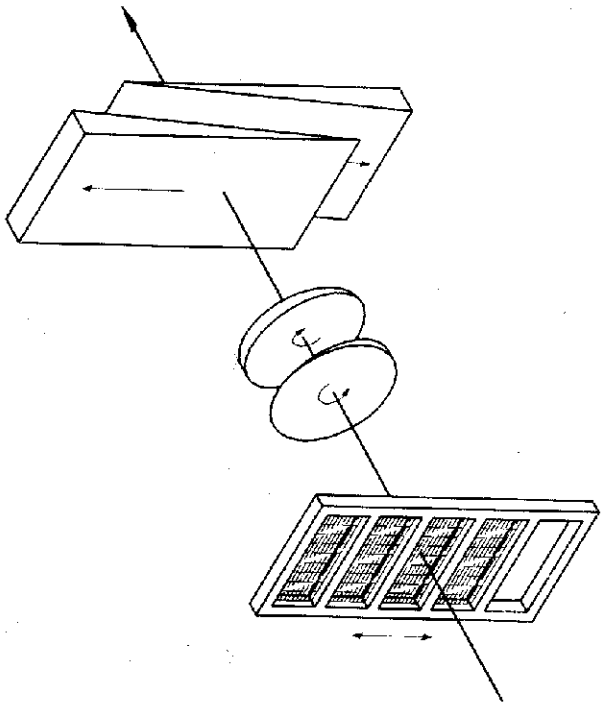

Fig. 8. Mechanical layout of the F_2-degrader system.

The degrader shape and the thickness have to be optimized for the specific requirements of each experiment and the degrader slope has to be readjusted for each selected isotope. It is therefore necessary to have a versatile and flexible degrader system operated by remote control. These requirements are fulfilled with the realization of the degrader system schematically shown in fig. 8 [8,31]. The ladder and the wedges of this array represent the homogeneous parts of the degrader, whereas the degrader slope along the x direction can be adjusted with two wedge-shaped discs rotating simultaneously in opposite directions. At relativistic energies the required degrader shape deviates only slightly from a linear approximation which is realized by this construction.

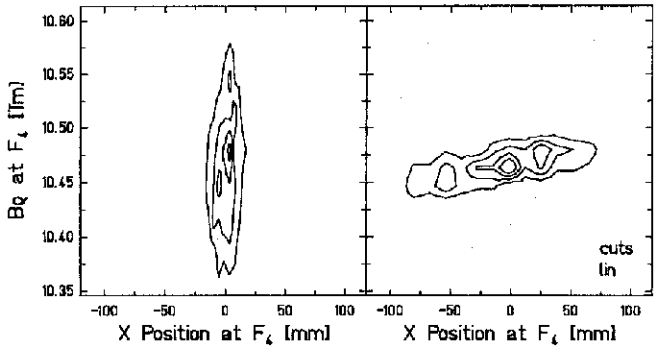

Fig. 9. The imaging by an achromatic (left-hand side) and a nearly monoenergetic (right-hand side) degrader in the $B\rho-x$ phase space illustrated with a fragment beam of ^{36}P produced by 1000 MeV/u ^{40}Ar in a 4 g/cm^2 Be target. The degrader thickness on the optical axis was half of the corresponding range of the selected fragments.

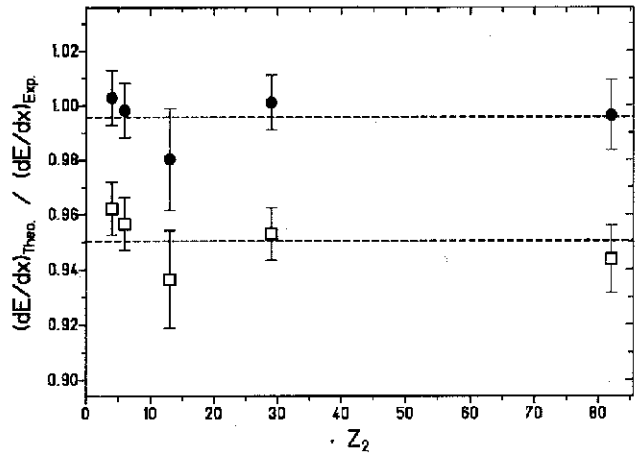

Fig. 10. Measured stopping-power values of 780 MeV/u ^{136}Xe compared with the relativistic Bethe theory (open squares) and the Ahlen theory (full circles). The dashed lines are to guide the eye.

Fig. 9 shows measured examples of phase-space imaging for a secondary beam of ^{36}P produced via fragmentation of 500 MeV/u ^{40}Ar. The degrader slope was changed such that a focus in x direction (achromatic degrader, left-hand side of fig. 9) or energy bunching (monoenergetic degrader, see right-hand side) were achieved. The achromatism of the FRS in combination with the degrader was verified with the striped target too (see above).

A precise knowledge of the atomic slowing-down properties of relativistic heavy ions is crucial to the successful application of the $B\rho-\Delta E-B\rho$ separation method. This statement becomes obvious if one keeps in mind that the momentum dispersion from F_2 to F_4 is 8.5 cm/%. A wrong energy-loss prediction for the F_2-degrader by a fraction of a percent can thus prevent the desired isotope from being detected at F_4. Therefore, stopping power (dE/dx) and range measurements have been incorporated into first experiments at the FRS. At relativistic energies, many complications in the theoretical description of heavy-ion stopping phenomena due to multiple charge-exchange processes are drastically reduced, since the ions carry only few electrons or are completely ionized.

The energy-loss experiments were carried out with the first two FRS sections. The position distributions of the ions were measured with multiwire proportional chambers placed at F_1 and F_2. In fig. 10 we present first results of dE/dx measurements of 780 MeV/u Xe ions in different monatomic solids. The experimental data are compared with the Bethe theory and also with the Ahlen theory including the higher-order correction terms to the first Born approximation [32]. The agreement of the experimental data with the Ahlen theory is very good for these projectile–target combinations, whereas the Bethe formula underestimates the

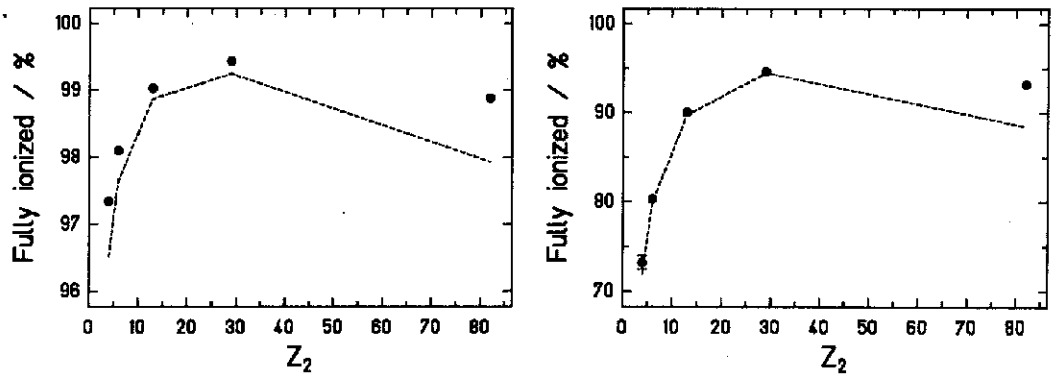

Fig. 11. Measured yields of fully stripped 800 MeV/u ^{136}Xe ions (left-hand side) and 1000 MeV/u ^{197}Au ions (right-hand side) in different target materials, compared with theoretical predictions (dashed lines), see text.

experimental results by about 5%. It is noteworthy that the achieved momentum-resolving power of the FRS was better than 3×10^{-4} in these measurements, which enables the energy loss to be determined to better than 1%. The target thicknesses were chosen to cause an energy loss less than 10% of the incident energy. The experimental results suggest that higher-order terms are indeed needed to improve the stopping theory for relativistic heavy ions. This conclusion is in accordance with the results deduced from range measurements performed at the BEVALAC [32].

The $B\rho$–ΔE–$B\rho$ method requires that the energy of each ion is high enough to ensure that multiple ionic charge states do not disturb the unambiguous $B\rho$-analysis. Therefore, we measured equilibrium charge-state distributions of relativistic ions that penetrated various target materials. These experiments were performed with the first FRS stage [33], where the magnitude of the dispersion allows the observation of at least two charge states simultaneously. The position distributions for all ions were recorded with the multiwire proportional chamber at F_1. In fig. 11 the experimental abundances of fully ionized 800 MeV/u Xe and 1000 MeV/u Au projectiles are shown for different target elements (Be, C, Al, Cu, and Pb) compared with the theoretical predictions [26] using the high-energy approach, i.e. assuming that only bare, H-, and He-like ions need to be considered [34]. The agreement between theory and experiment is remarkable except for that obtained with Pb targets where a higher degree of electron stripping than predicted was observed. Besides the interesting atomic physics aspects of these measurements, we conclude that a medium-Z production target should be used for fragmentation products using the heaviest projectiles in order to avoid contaminations due to the different charge states.

In order to verify the isotopic resolution of the FRS by means of the $B\rho$–ΔE–$B\rho$ method, ^{36}P fragments from 500 MeV/u and 1000 MeV/u Ar + Be reactions were investigated. The measured separation quality is in excellent agreement with our calculations [26], see fig. 12. The degree of difficulty in separating secondary beams was then gradually increased. We used Kr, Xe, and Au beams to test the design goals and to study the physics limitations that determine the production and isotopic separation of relativistic projectile fragments. In the following, we discuss representative results obtained with Au projectiles. A 1 GeV/u gold beam was fragmented in an 1.4 g/cm^2 Al target. The choice of the target material was guided by the results of the above-mentioned charge-state measurements. The FRS was tuned to separate ^{188}Pt isotopes using a 5.6 g/cm^2 Al degrader at F_2. The position distributions, shown in

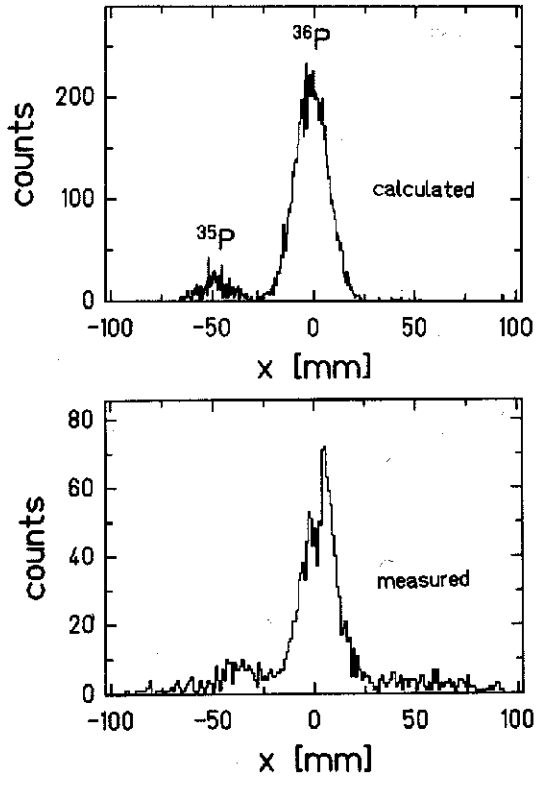

Fig. 12. Measured separation of ^{36}P produced by 1000 MeV/u ^{40}Ar in Be using an achromatic degrader at F_2. The data are compared with our MOCADI calculations.

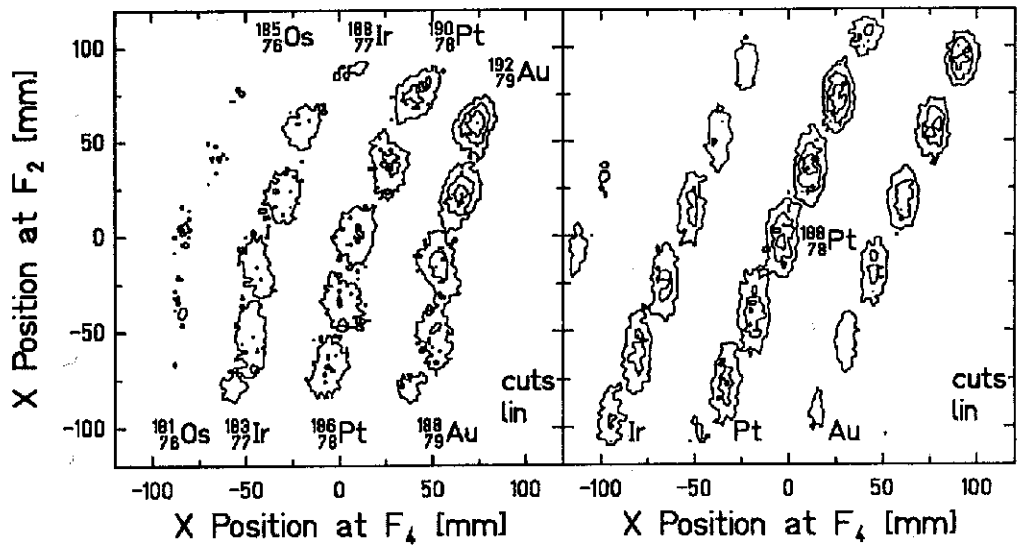

Fig. 13. Measured (left-hand side) and calculated (right-hand side) position distributions of fragments produced by 1000 MeV/u ^{197}Au in 1.4 g/cm^2 Al. The FRS was tuned to separate ^{188}Pt ions.

fig. 13 (left-hand side), were recorded in coincidence at F_2 and F_4. The results clearly demonstrate that by introducing slits at both focal planes a single isotope can be provided at F_4. It should be noted that this is the first time that isotopic separation for such heavy relativistic projectile fragments has been achieved. The experimental results are compared with the calculations performed with MOCADI [26] (see right-hand side of fig. 13). The overall agreement between experiment and simulation is very good. The slight bending observed in the experimental data within each element is probably due to residual image aberrations.

4. Conclusions and outlook for the experimental program

In this report we have presented the ion-optical and technical characteristics of the FRS and have shown first results on the separation of relativistic nuclear fragments using the high-resolution achromatic mode. The isotopic separation of heavy relativistic fragments produced by xenon and gold projectiles was performed for the first time. Although the experiments were mainly aimed at verifying the ion-optical properties of the FRS and studying the separation power of the $B\rho$–ΔE–$B\rho$ method and the corresponding physical processes, several exotic isotopes were already identified. The deduced nuclear cross section data are in good agreement with the empirical parametrization EPAX and allow a more reliable prediction of production rates for exotic species.

Our first experiments in atomic physics were aimed at ionic charge-state and energy-loss measurements. The data on ionic charge states confirm the results obtained at the BEVALAC [34] and verify the validity of theoretical models implemented in our simulations. The energy-loss measurements proved successful due to the excellent performance of FRS. Obviously higher-order correction terms to the Bethe theory are necessary to improve agreement between theory and experiment.

The different dipole stages of the FRS offer an ideal condition for particle–photon coincidences, because one can prepare and select the desired charge-exchange events. The atomic physics program at the FRS will concentrate in the next experiments on the spectroscopy of few-electron systems and on the investigations of resonant electron capture processes in amorphous light-Z targets and in single crystals under channeling conditions. The use of cooled beams from the ESR will open a new field for channeling studies using relativistic heavy ions [35]. The high energies at SIS allow for the first time experiments on the resonant coherent excitation of both nuclear and atomic levels in stable or even in radioactive atoms produced and separated at the FRS.

Radioactive beams produced and separated by the FRS have a wide field of applications. An applied physics experiment has been conducted by using the separated ^{19}Ne beam created by fragmentation of 400 MeV/u ^{20}Ne in Be. The degrader shape was chosen to bunch the energy distribution of the fragment beam. Its decay properties enabled us to use this fragment beam as a diagnostic tool after implantation. Range distribution were measured with a positron emitter camera [36]. This was a first investigation at the FRS in the field of radiation biophysics, and this project will be continued with light projectile beams.

The future FRS experimental program for nuclear physics will be characterized by the production and investigation of exotic nuclei complemented by reac-

tion studies. The study of neutron and proton rich nuclei will be continued to understand problems central to nuclear structure and astrophysics. In this field we will perform an experiment to produce neutron-halo nuclei (e.g. ^{11}Li) in the reaction ^{18}O + Be and investigate the nuclear structure via secondary reactions using the large neutron detector LAND [37]. In the near future SIS will provide uranium beams which allow us to extend our fragmentation studies up to the heaviest ions. Uranium fragments will be studied also in secondary reactions via electromagnetic dissociation.

The combination of the FRS with the ESR will open a new field with secondary beams of high phase-space density. The excellent performance of the electronic cooling facilities in the ESR has been demonstrated recently for stable beams of Ne, Ar, Kr, and Bi [4]. The momentum spread of less than 10^{-5} and the transverse emittance of 0.05π mm mrad are basic preconditions for the planned high-resolution experiments. Examples of such investigations are direct mass measurements and nuclear structure studies with direct reactions in light targets, i.e. (d,p)- and (p,p')-scattering with exotic nuclei cooled in the ESR.

Acknowledgements

We would like to thank the accelerator staff, the team of the target lab and the team of the mechanical workshops for their support in achieving the experimental results presented here. Y. Fujita and D.J. Vieira express their gratitude to the Alexander-von-Humboldt Foundation for the support during their stay in Germany. It is a pleasure to thank Ms. U. Vogel for typing the manuscript.

References

[1] K. Blasche, SIS Beam Development 1989–1991, GSI-Report GSI-SIS-INT/86-2.
[2] H. Geissel et al., Projectile Fragment Separator, A proposal for the SIS-ESR experimental program (1987); and GSI Report GSI-89-30 (1989);
G. Münzenberg et al., Proc. 1st Int. Conf. on Radioactive Nuclear Beams (World Scientific, Singapore, 1990) p. 91.
[3] B. Franzke, Nucl. Instr. and Meth. B24/25 (1987) 18.
[4] F. Bosch, Nucl. Instr. and Meth. A314 (1992) 269.
B. Franzke, S. Baumann, K. Beckert, H. Eickhoff, B. Francak, A. Gruber, F. Nolden, U. Schaaf, H. Schulte, P. Spädtke, M. Steck and J. Struckmeier, Proc. 1991 Particle Accelerator Conf., San Francisco, USA.
[5] K.L. Brown, D.C. Carey, Ch. Iselin and F. Rothacker, CERN Report 80-04 (1980); CERN Report 74-2 (1974).
[6] A. Schröter et al. Sci. Rep. GSI-92-1 (1992).
[7] O. Klepper et al., these Proceedings (EMIS-12) Nucl. Instr. and Meth. B70 (1992) 427.
[8] H. Folger, H. Geissel, W. Hartmann, J. Klemm, G. Münzenberg, D. Schardt, K.-H. Schmidt and W. Thalheimer, Nucl. Instr. and Meth. A303 (1991) 24.
[9] C. Ziegler, T. Brohm, H.G. Clerc, H. Geissel, K.-H. Schmidt, K. Sümmerer, D.J. Vieira and B. Voss, Sci. Rep. GSI-91-1 (1991) p. 291.
[10] R. Anne, C. Bruske, K. Burkhard, M. Fradj, H. Geissel, Y. Georget, R. Hue, R. Johänntges, R. Kirchner, A.C. Mueller, E. Roeckl, J. Rasmusson, K. Rykaczewski and M. Weber, Sci. Rep. GSI-90-1 (1990) p. 257.
[11] M. Steiner, Diplomarbeit, TH Darmstadt (1991).
[12] G. Münzenberg, these Proceedings (EMIS-12) Nucl. Instr. and Meth. B70 (1992) 265.
[13] T.J.M. Symons, Y.P. Viyogi, G.D. Westfall, P. Doll, D.E. Greiner, H. Faraggi, P.J. Lindstrom, D.K. Scott, H.J. Crawford and C. McParland, Phys. Rev. Lett. 42 (1979) 40.
[14] G.D. Westfall, T.J.M. Symons, D.E. Greiner, H.H. Heckman, P.J. Lindstrom, J. Mahoney, A.C. Shotter, D.K. Scott, H.J. Crawford, C. McParland, T.C. Awes, C.K. Gelbke and J.M. Kidd, Phys. Rev. Lett. 43 (1979) 1859.
[15] I. Tanihata, in: Treatise on Heavy Ion Science, vol. 8, ed. D.A. Bromley (Plenum, New York, 1989) p. 443.
[16] J.P. Dufour, R. Del Moral, A. Fleury, F. Hubert, D. Jean, M.S. Pravikoff, H. Delagrange, H. Geissel and H.-H. Schmidt, Z. Phys. A324 (1986) 487.
[17] R. Anne, D. Bazin, A.C. Mueller, J.C. Jacmart and M. Langevin, Nucl. Instr. and Meth. A257 (1987) 215.
[18] B.M. Sherrill, D.J. Morrissey, J.A. Nolen Jr. and J.A. Winger, Nucl. Instr. and Meth. B56/57 (1991) 1106.
[19] D.J. Morrissey, Phys. Rev. C39 (1989) 460.
[20] H. Geissel, G. Münzenberg, J.P. Dufour, B. Franczak, K.-H. Schmidt, D. Schüll and P. Armbruster, Proc. Workshop on Accelerated Radioactive Beams, Parksville, Canada, 1985, TRI-85-1, p. 341.
[21] M. Pfützner, B. Voss, H.-G. Clerc, H. Geissel, G. Münzenberg, F. Nickel, K.-H. Schmidt, M. Steiner, K. Sümmerer and D.J. Vieira, Sci. Rep. GSI-91-1 (1991) p. 288.
[22] B. Voss, Diploma Thesis, TH Darmstadt (1989).
[23] M. Weber et al., to be published.
[24] Zhan Wenlong, G. Audi, L. Bianchi, A. Cunsolo, H. Dumont, B. Fernandez, A. Foti, J. Gastebois, A. Gillibert, W. Mittig, M. Morjean, Y. Pranal, Y. Schutz and C. Stephan, Nouvelles du GANIL 25 (1988) 22.
[25] K. Sümmerer, W. Brüchle, D.J. Morrissey, M. Schädel, B. Szweryn and Yang Weifan, Phys. Rev. C42 (1990) 2546.
[26] Th. Schwab, GSI Report GSI-91-10 (1991).
[27] J.P. Dufour, R. Del Moral, H. Emmermann, F. Hubert, D. Jean, C. Poinot, M.S. Pravikoff, A. Fleury, H. Delagrange and K.-H. Schmidt, Nucl. Instr. and Meth. A248 (1986) 267.
[28] K.-H. Schmidt, H. Geissel, G. Münzenberg, E. Hanelt and J.P. Dufour, Nucl. Instr. and Meth. A260 (1987), 287.
[29] B. Blank, J.J. Gaimard, H. Geissel, G. Münzenberg, K.-H. Schmidt, H. Stelzer, K. Sümmerer, H.G. Clerc, E. Hanelt, B. Voss, D. Bazin, R. Del Moral, J.P. Dufour, A.

Fleury and M.S. Pravikoff, Nucl. Instr. and Meth. A286 (1990) 160.
[30] H. Geissel, Th. Schwab, P. Armbruster, J.P. Dufour, E. Hanelt, K.-H. Schmidt, B. Sherrill and G. Münzenberg, Nucl. Instr. and Meth. A282 (1989) 247.
[31] J. Weckenmann, E. Hanelt and K.-H. Schmidt, GSI Report GSI-90-13 (1990).
[32] S.P. Ahlen, Rev. Mod. Phys. 52 (1980) 121 and references therein.
[33] Th. Stöhlker, H. Geissel, H. Folger, C. Kozhuharov, P.H. Mokler, G. Münzenberg, D. Schardt, Th. Schwab, M. Steiner, H. Stelzer and K. Sümmerer, Nucl. Instr. and Meth. B61 (1991) 408.
[34] R. Anholt, W.E. Meyerhof, X.-Y. Xu, H. Gould, B. Feinberg, R.J. Mcdonald, H.E. Wegner and P. Thieberger, Phys. Rev. A36 (1987) 1586;
R. Anholt, Phys. Rev. A31 (1985) 3579.
[35] H. Geissel, GSI Report GSI-91-37 (1991); Nucl. Instr. and Meth. B67 (1992) 120.
[36] W. Enghardt, W.D. Fromm, P. Manfraß, J. Pawelke, M. Sobiella, H. Geissel, D. Schardt, H. Keller, G. Kraft, A. Magel, G. Münzenberg, F. Nickel, M. Pfützner, B. Voss, C. Sastri, to be published.
[37] H. Emling, GSI Nachrichten 5-89 (1989).